

Effect of Nb Content on Behavior of (Ti-Nb) Shape Memory Alloys for Biomedical Applications

Sura Ali Shahee*, Ekbal mohammed Saeed salih, Nabaa Sattar Radhi

College of Materials Engineering, University of Babylon, Iraq

Received 29 Nov 2023

Accepted 25 Apr 2024

Abstract

Titanium–niobium (Ti–Nb) binary alloys have lately been given attention and attraction due to their non-toxic properties and low Young's modulus. All alloys manufactured by powder metallurgy and studied through the influence of Nb content (13, 14, 15, 23, 24 and 25) at% on the shape memory effect, the surfaces properties (Vickers microhardness, Contact angle (CA), Scanning Electron Microscopy (SEM) and X-ray diffraction (XRD), DSC and Corrosion resistance (in Hank solution) of Ti–xNb alloys). The results of XRD illustrated that the (Ti–xNb) alloys included α'' and β Ti phases, such that as the amount of Nb in the alloy increased the β phase increased proportionately. Regarding the shape memory effect (SME%) of alloys, the treatment was determined by using microhardness after and before the heat treatment, according to the result of DSC test, by two different temperature (50 and 150) °C in which the result was far less than 5%.

All Ti–xNb alloys displayed noticeably higher hardness, compressive strength and decreased contact angle, low Corrosion was founded on Ti–xNb alloys in hank solutions. In overall, binary Ti–xNb at% alloys are a suitable candidate for dental and orthopedic implants owing to their enhanced mechanical characteristic and Biological performance that is comparable.

© 2024 Jordan Journal of Mechanical and Industrial Engineering. All rights reserved

Keywords: Binary Titanium–Niobium, Powder metallurgy, Shape memory alloys, Hank solution, Orthopedic and Dental implants.

1. Introduction

For Biomedical applications, the shape memory alloys (SMA) with superior biocompatibility are important. Because its excellent corrosion resistance, shape memory ability, and superelasticity, Ti-Ni SMA have been employed successfully as medical materials [1]. But, the toxicity and hypersensitivity of Ni were noted in Ti-Ni alloys [2-4].

To achieve safety completely, the making use of Ni-free Ti-based SMA is necessary. It is well-known that Ti alloys of β -type undergo a martensitic change from body centered cubic (BCC) β parent phase to one of Two metastable structures: either orthorhombic Martensite (α'') or hexagonal Martensite (α'). At specific concentration of elements of alloy, the martensite structure transforms from the β to α'' . Internal twinning is typically used to accommodate the strain of transformation from the β to α'' . The reversion of α'' to β in β Ti alloys is linked to the shape memory effect [5-7].

By adding alloying components, the martensitic transformation starts temperature (M_s) can be altered. However, alloy design containing non-toxic elements is needed for biological applications. At 882 °C, the α -phase of pure Titanium low temperature HCP (Hexagonal Close Packed) changes to the β -phase. The High-temperature β -phase can be stabilized at ambient temperature by the addition of elements like Nb, Mo, and Ta [8-10].

In the Ti-Nb system, when adding one atomic percentage of Nb to the β -Ti alloy, the temperature of M_s dropped by 40 °C [11,12]. Ti-26Nb has a theoretical (crystallographic) recovery strain of 3%. [9]. This value can be raised by either lowering the Nb concentration or by substituting Ta, Zr, or Mo for Nb[13]. The comprehensive research concentrates on shape-memory properties of Ti-Nb-based alloy produced by cold-working and casting methods. As an illustration, Kim et al. [9] observed that the greatest recovery strain 4.2% in a 400 °C-aged cold-rolled Ti-26Nb alloy, Mehmet Kaya et al. [14] indicated that as green compact grew, porosity reduced, and as porosity declined, ultimate compression rose up to 900 MPa. All samples of Ti-18Nb alloys also exhibit the phases, and a trace amount of martensite. Jian Zhang et al. [15] Examined changes in phase upon heating at various heating rates in quenched Ti-(16–25%) Nb HTSMAs were characterized. In contrast, (the beginning temperature of the $\alpha'' \rightarrow \beta$ transition) does not grow linearly with decreasing Nb-content.

In this work, mechanical characteristic and shape memory behavior of (Ti- xNb) alloys (which produced by powder metallurgy) were studied to create Ni-free SMA used in biomedical application. Compressive, hardness and shape memory effect tests were used to examine the impacts of Nb content on shape memory behavior and mechanical properties. The effect of heat treatment on shape memory property were also investigated. The measurements of XRD were made at room temperature to identify the constituent

* Corresponding author e-mail: sura.alshahee@gmail.com.

phases and SEM, DSC, corrosion resistance (in hank solution).

2. Experimental Part

The average particle size and materials purity of (Ti-Nb) alloys powders used when preparing are explained in table 1.

Table 1. The average particle size and Purity of powders

Powder	Average particle size(μm)	Purity%	Origin.
Titanium	25.16	99.6	Fluke -swiss
Niobium	5.07	99	-company in china.

Powder metallurgy was used to prepare the specimens. When the mix of Ti and Nb, ($x=13, 14, 15, 23, 24$ and 25) at percent is utilized, a delicate balancing is employed to measure the powder's weight. The next step, the weighed powder mixture placed in the planetary automatic ball mill about 5 hr to accomplish a fine and uniform dispersion of powder particles. A 2 g powder combination was compressed with a cylindrical die in an electrical hydraulic press in one direction to prepare a sample disk with dimensions of 3 mm in thickness and 12 mm in diameter (hardness, corrosion, and microstructure). An interior lubricant made from graphite has been included into the die walls to lessen pressing friction. Compacting involved applying 800 MPa. After being crushed in green, the samples were sinter in a tube furnace. The specimens were subjected to an argon atmosphere during the sintering process to prevent oxidation. Following a seven-hour sintering procedure at 1300°C , the sintered samples are continually purged with argon and allowed to gradually cool in the furnace until they are close to ambient temperature. After the sintering process, the sintered sample have been gone through heat treatment process involved heating to 1200°C and holding it at this temperature for 1 hour then rapidly cooling in iced water, Table (2) explains the composition and code of alloys that were used in this work.

Following sintering, in order to grind each sample, silicon carbide sheets with granularity of (180, 220, 320,400, 600, 800, and 1500). The surfaces were then polished with a diamond using 10 μm diamond paste and metallographic polishing pads to achieve a wonderful mirror finish. After that, polished samples were etched for 10 to 15 seconds in Kroll's solution (3mL HF, 6mL HNO₃, and 100mL H₂O) [16]. After the etching procedure, the samples were cleaned with water and dried.

3. Tests

For the purpose of identifying the crystal structures of constituent phases:

- X-ray diffraction (XRD) research was done on finely polished samples.
- Samples were analyzed by scanning electron microscopy (SEM) and (EDS).
- Differential Scanning Calorimeter (DSC): This test is used to determine the transformation temperatures for

alloys, the base specimen of weight 15 mg was warmed up to 100°C , after which it underwent cooling to -50°C .

- Also, the shape memory effect can be calculated depending on the transformation from β to α' and vice versa, there was shape memory effect of the specimen determined by Vickers hardness. The hardness of specimen is calculated through determining the dimensions of impression of Vickers hardness at room temperature. The specimen was placed in a vacuum furnace for 2 hr at (50 and 150) $^{\circ}\text{C}$. The dimension of the impression after drying was measured using the following equation [17]:

$$\text{SME} = \frac{db - da}{db} * 100\% \quad (1)$$

Where: db = diameter of impression in μm before heat treatment.

da = diameter of impression in μm after heat treatment.

- All samples had their Micro-hardness testing which was used to measure the hardness values by (a Digital Micro hardness tested HV-1000) with weights of 200 g for 10 s; The values given are the three measurements' averages.
- The samples' dimensions (12 mm * 18 mm) are utilized to determine their compression strength. Throughout the whole test, a constant loading rate of 0.5 mm/min was utilized. The compressive strength is calculated using the formula given in equation [18]:

$$\text{Compressive strength (MPa)} = \frac{\text{maxforce (N)}}{\text{cross sectional area (mm}^2\text{)}} \quad (2)$$

- Also, contact angle test was accomplished to evaluate the effect of additives on the wettability of pure materials by means of contact angle range (0 to 180°) through using a device which makes calculation of contact angle and the mean values, and displays a real-time data graph while videotaping variations in contact angle.
- To understand the corrosion behavior in the human body, all the corrosion experiments on specimens performed in Hank's solutions were employed in this test. The SCE, Pt, and sample were utilized in accordance with the ASTM standard as the working electrodes and counter reference respectively. The polarization curves for potentiodynamics were achieved and Tafel plots were used to determine the corrosion potential and corrosion current density (I_{corr}) using the potential of the anodic and cathodic branches, which is 250 mV below and above the potential of an open circuit, the scanning was kept going. The following equation used to measure the corrosion rate according to [19]:

$$\text{Corrosion rate(mpy)} = \frac{0.13 I_{\text{corr}}(Ew)}{\rho} \quad (3)$$

Where mpy, Ew , I_{corr} , and ρ , represent (mpy) (mills per year), the equivalent weight (g/eq), current density (A/cm^2), density (g/cm^3), respectively.

The metric and time conversion factor equal to 0.13.

4. Results and Discussion

4.1. X-Ray Diffraction analysis.

Figure 1 shows the XRD patterns for the alloys A, B, C, D, E, and F after sintering. the phases (α' Ti and β Ti) created

from the Ti and Nb. This shows that 1300°C for 7 hours under Argon gas was adequate to complete the process of sintering as a result of a rise in the interdiffusion within Ti and Nb.

The phase analysis, demonstrated in Figure (1), indicates that the regular β phase is observed and increase intensity with increase niobium content also α'' phase is observed, which is in good agreement with research [20]. When Nb content is increased to 25 at. %, the peaks of martensitic phases disappear and β phase becomes the dominating one.

4.2. Microstructure of Ti-Nb Alloys

By using a scanning electron microscope (SEM), the microstructure of the etched specimens was discovered. The specimens were etched to show the microstructure's grain boundaries. There are irregular, round pores of different

sizes and the microstructure of specimens have two phases (β Ti and α'' Ti) can be seen, supporting the XRD data. The results of SEM shown in figures (2-7), On the basis of the X-ray diffraction analysis results, all samples owned the α'' and β phases and demonstrated that the β phase rose as the niobium content did [20]. These images illustrate a presence α'' phase, plate-like. Niobium content had a larger effect on the grain size and the volume fraction of the plates. Therefore, The volume fraction of the plates increased with increasing Niobium. The solid plates of α'' phase were observed in D, E, F alloys as indicated in figures (5-7) which are thicker and deeper, and therefore the range of transformation degrees decrease with the increased niobium.

The composition of all alloy analysis by the elemental mapping of EDS which can be shown in figures (8-9).

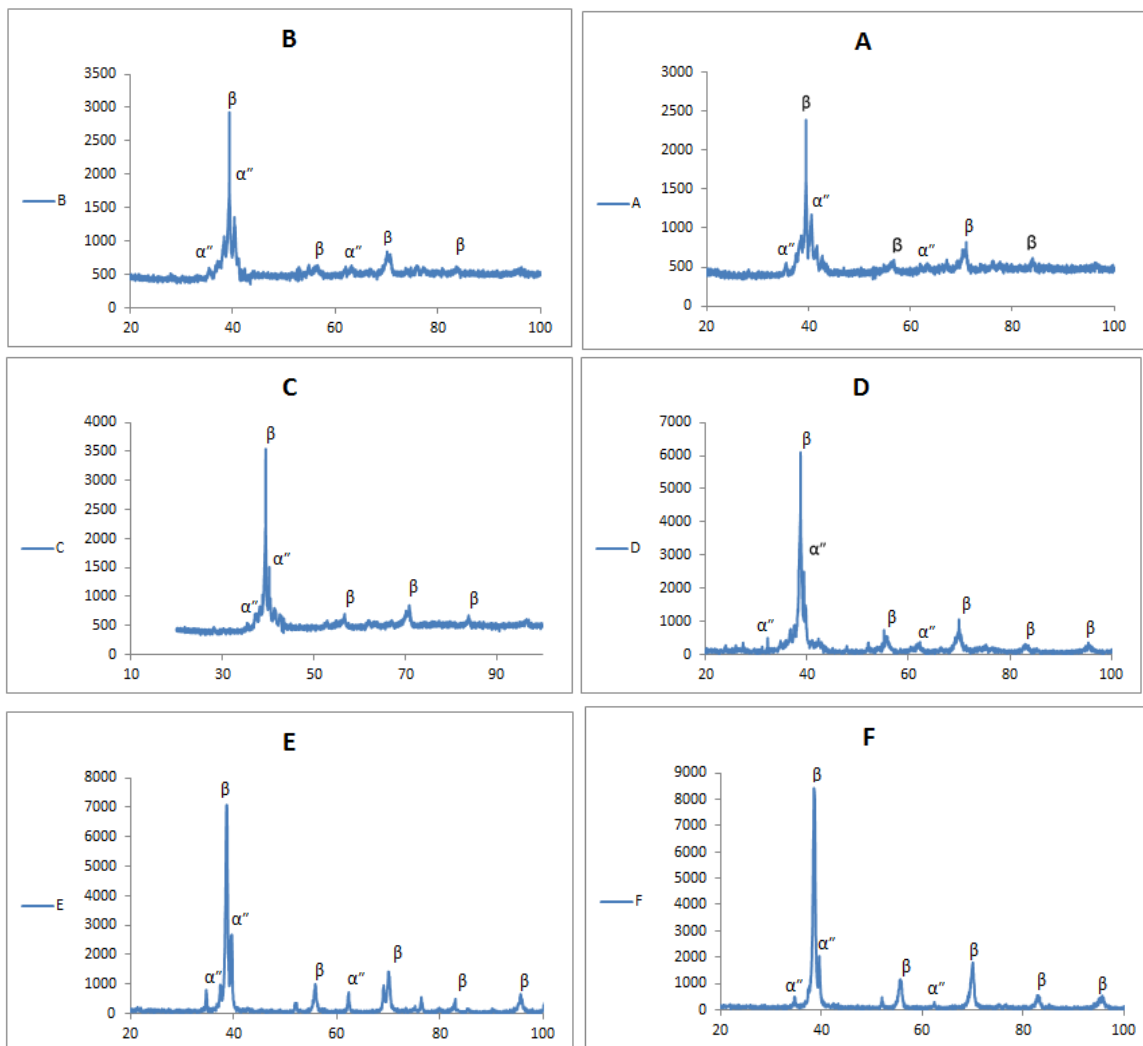


Figure 1. Show the patterns of XRD for all alloys.

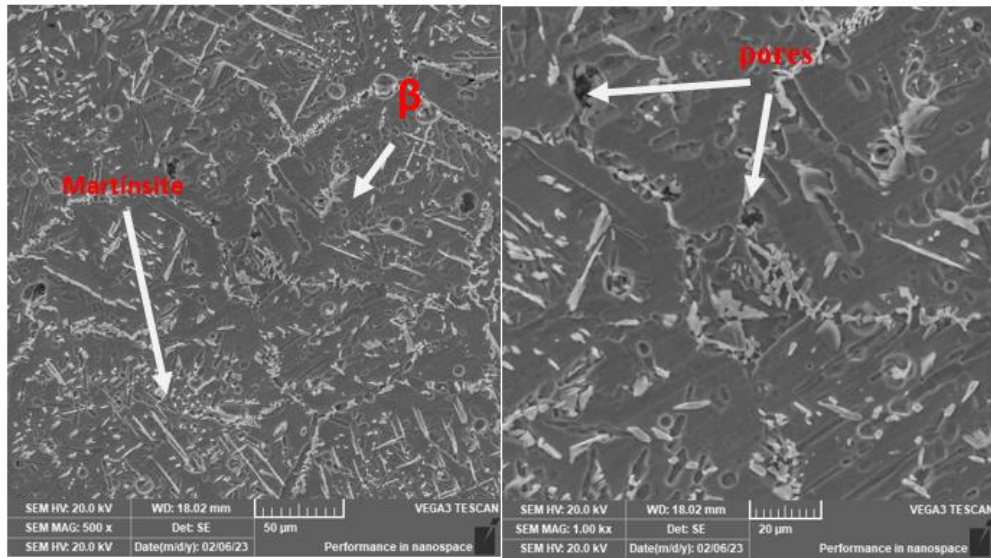


Figure 2. The SEM image for (A) layer alloy.

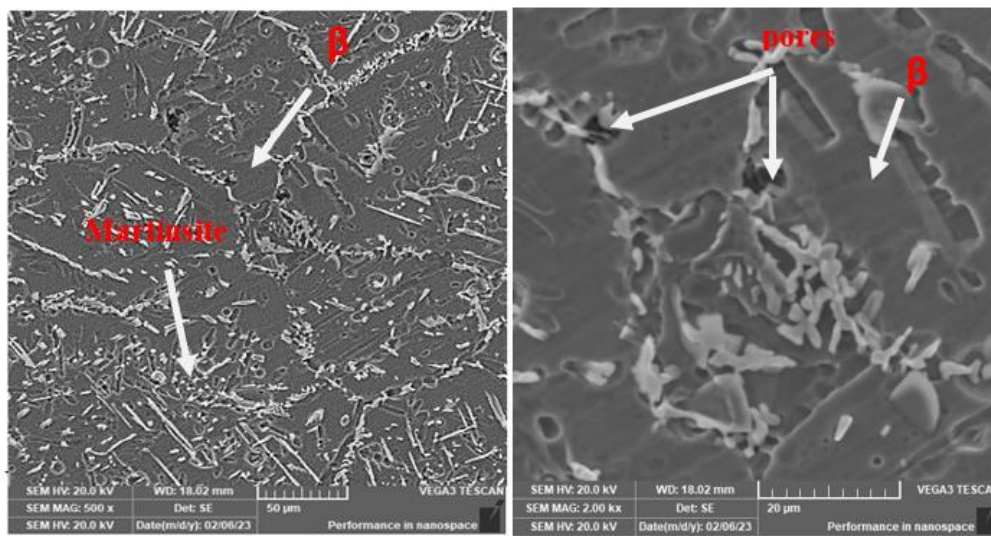


Figure 3. The SEM image for (B) layer alloy.

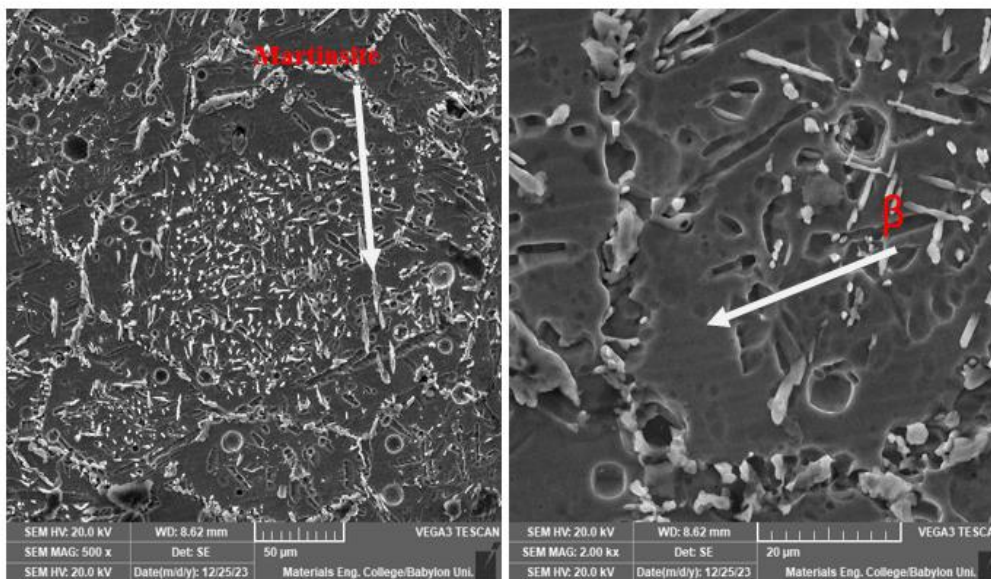


Figure 4. The SEM image for (C) layer alloy.

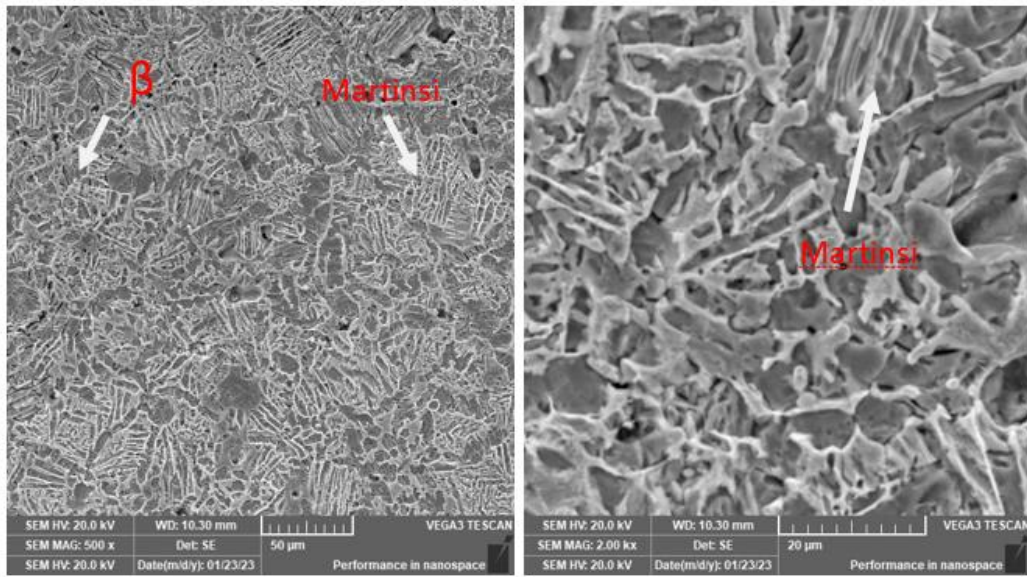


Figure 5. The SEM image for (D) layer alloy.

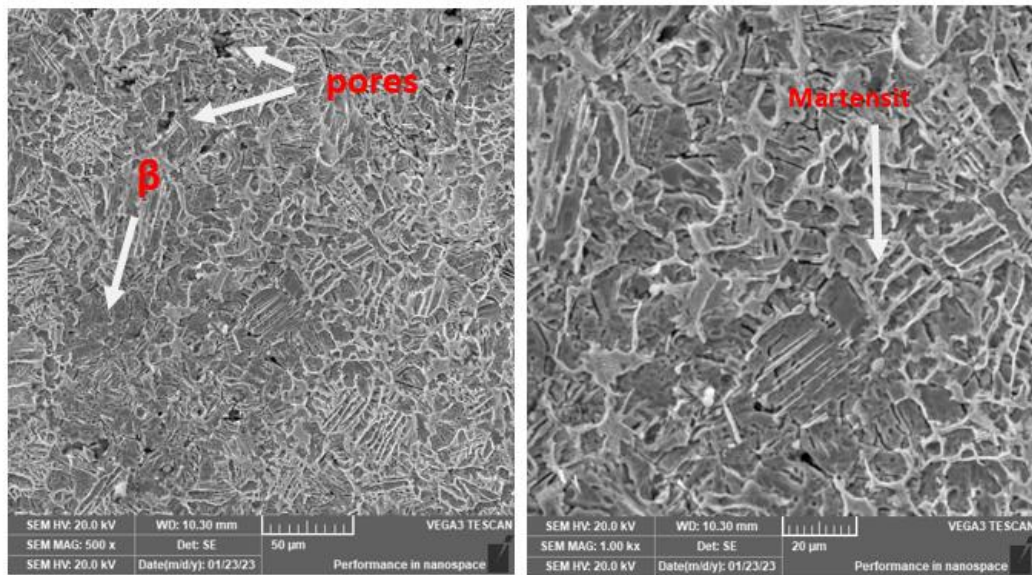


Figure 6. The SEM image for (E) layer alloy.

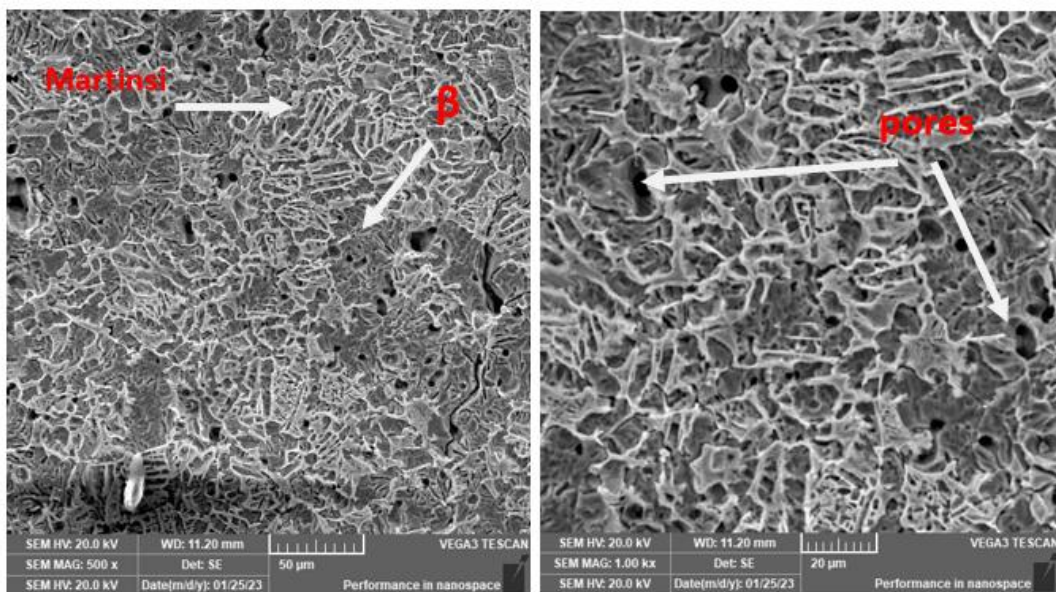


Figure 7. The SEM image for (F) layer alloy.

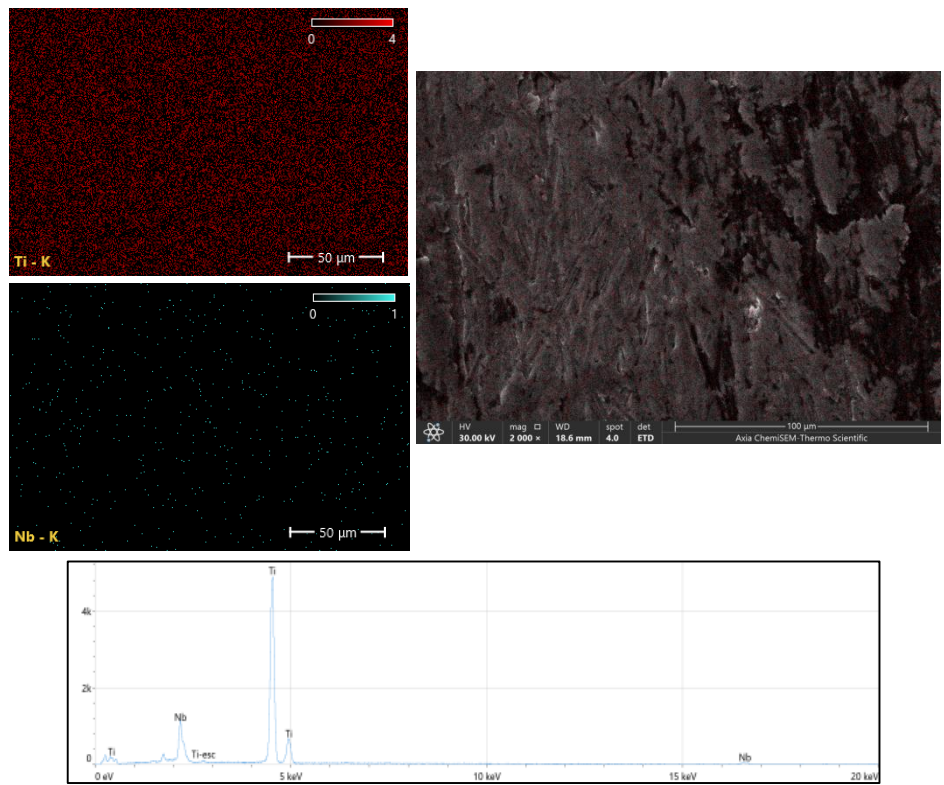


Figure 8. An EDS spectrum and chemical composition for A alloy.

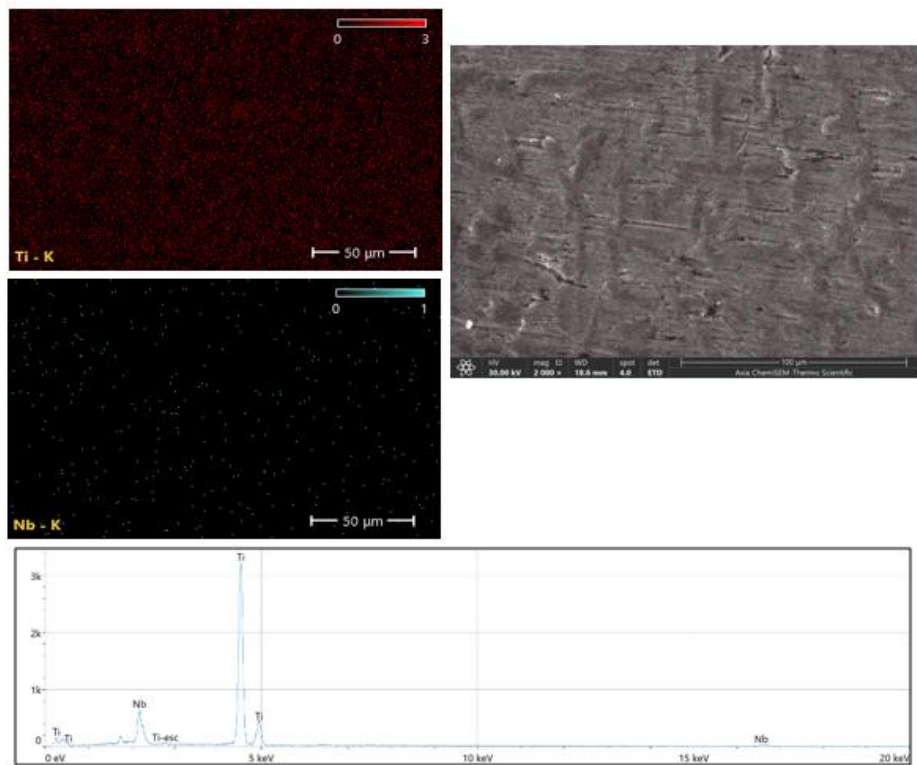


Figure 9. An EDS spectrum and chemical composition for B alloy.

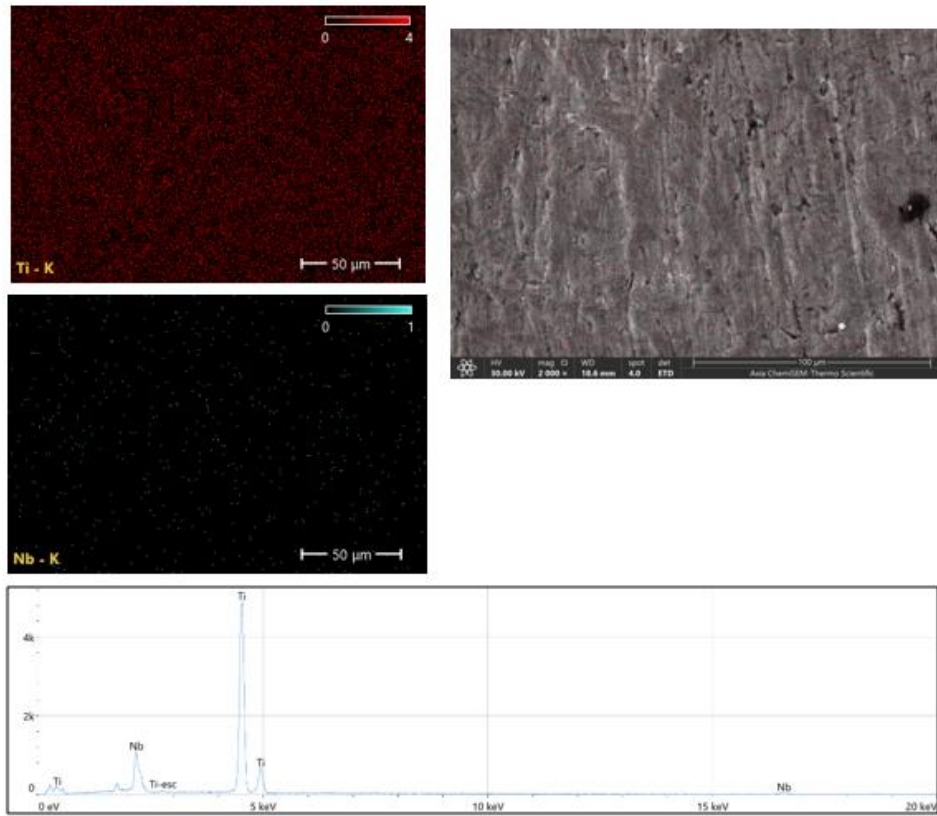


Figure 10. An EDS spectrum and chemical composition for C alloy.

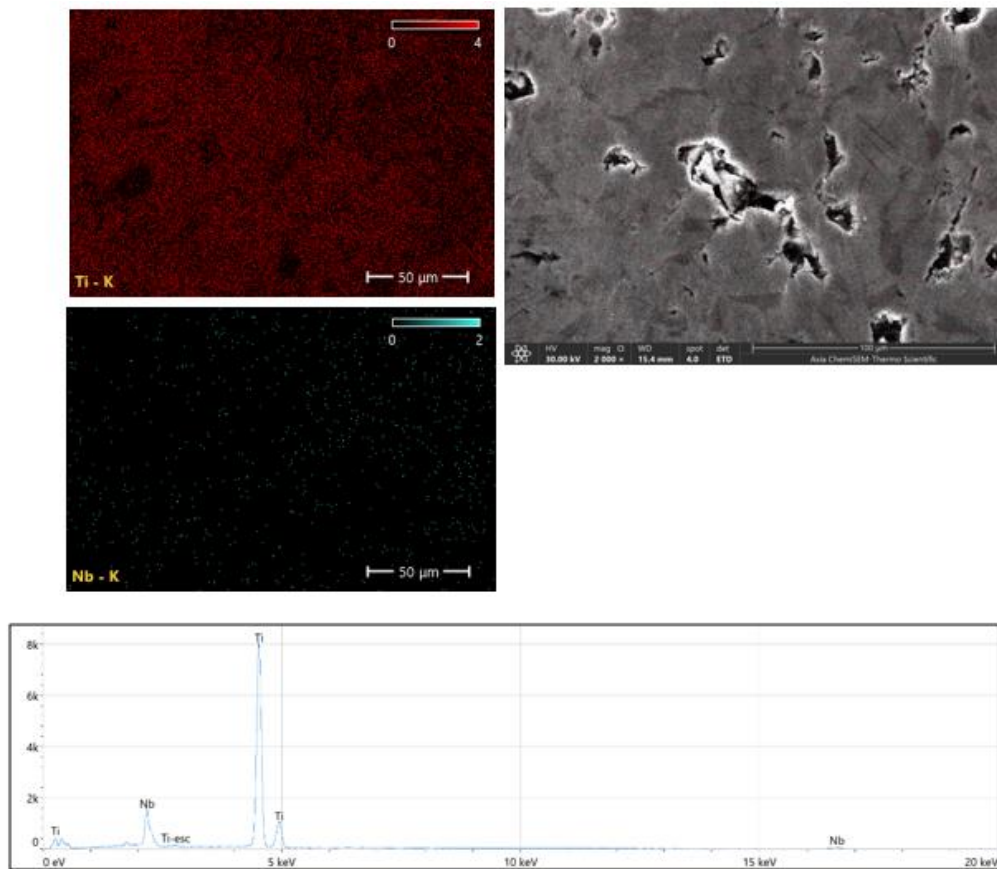


Figure 11. An EDS spectrum and chemical composition for D alloy.

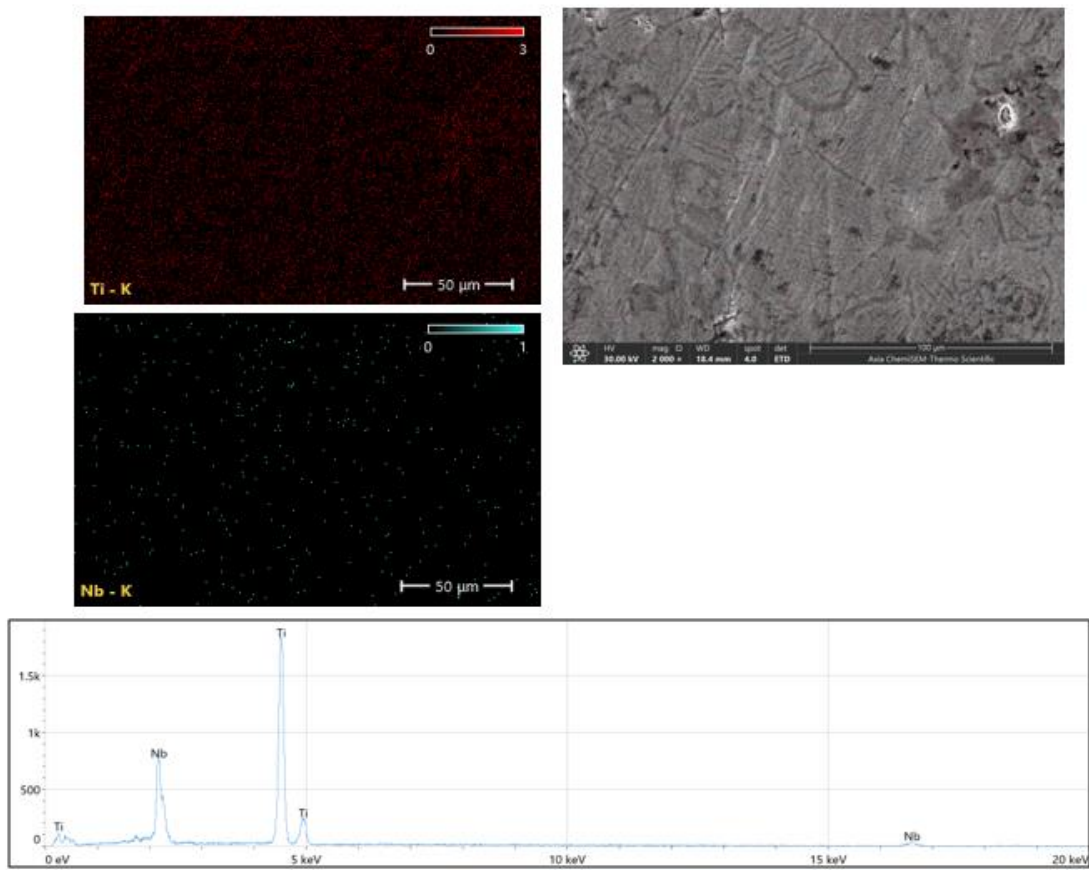


Figure 12. An EDS spectrum and chemical composition for E alloy.

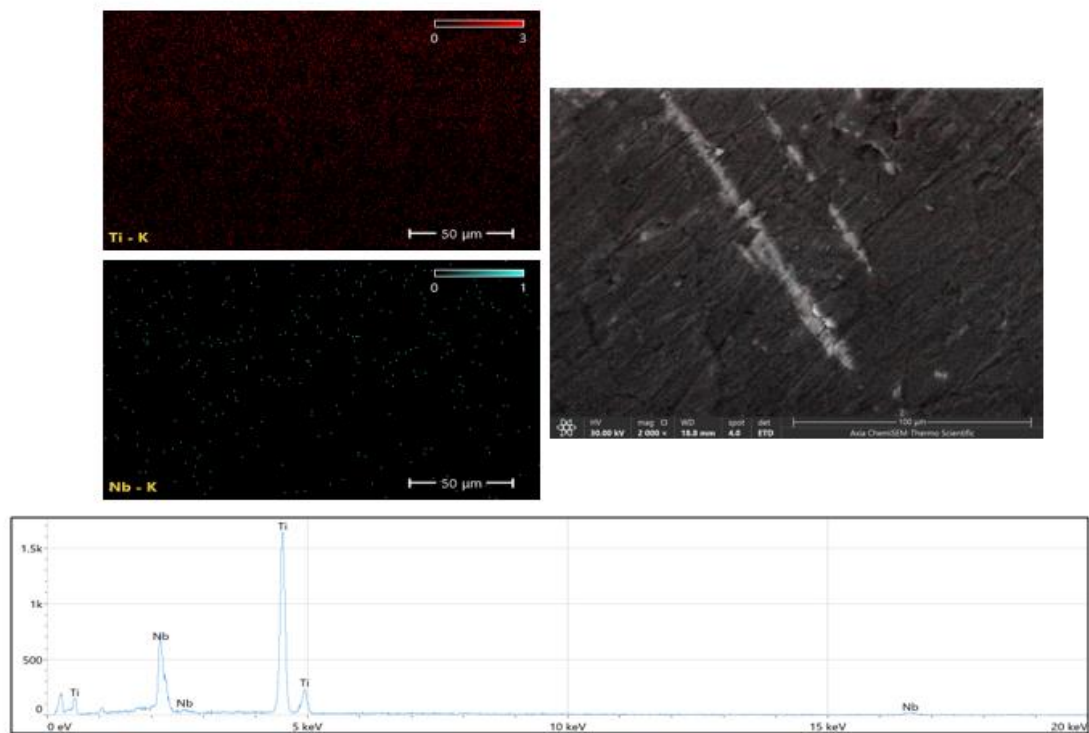


Figure 13. An EDS spectrum and chemical composition for F alloy.

4.3. Shape memory properties.

4.3.1. Differential scanning calorimeter (DSC) analysis measurements

All sintered Ti-Nb alloys (A, B, C, D, E, and F) were subjected to DSC measurements to determine the reversible β - α'' phase transformation. Figures (14–19) showed the DSC curves of previous alloys. It is clear that when sintered alloys are heated repeatedly, phase change peaks appear. The Ms of A, B and C measured from the curves are (-4.5, -20.5 and -29.3) °C respectively while the Ms of D, E, F alloy are higher which are (134.3, 137 and 133.1)°C. According to the results, it was found that when the niobium content is low, the transformation degrees are low.

Thermal analysis was done to determine the temperature region at which the studied alloys underwent reversible martensitic transition. The figures illustrate the Ti-Nb alloy's DSC heating and cooling curves which were estimated based on the alloy's As, Af, Ms and Mf temperatures. These results agree with other papers, such as Lai et al.'s [21] showing of martensitic transformation. From that, it is seen that a small difference in the chemical composition results in a change in the transformation temperature and thus can be seen in all temperatures in the range of martensite transformation and the Temp.hysteresis in Table (3), Where The Temp.hysteresis decreases with decreasing niobium content, where this agrees with the SEM figures.

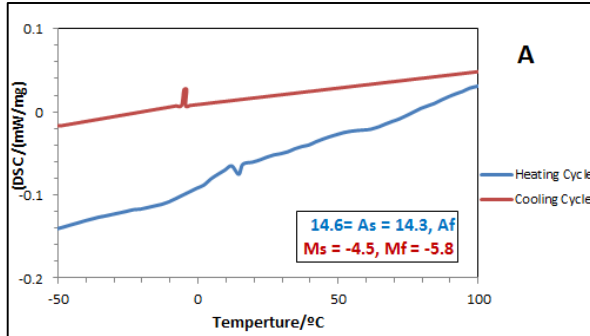


Figure 14. Typical DSC curve for A alloy.

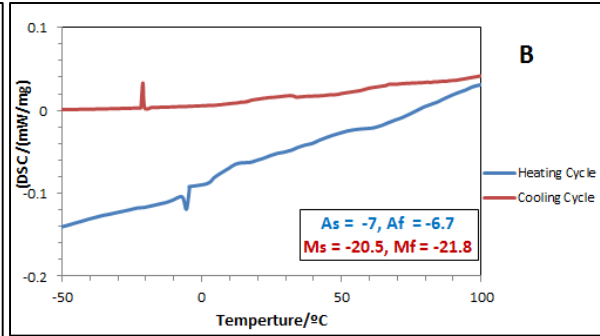


Figure 15. Typical DSC curve for B alloy.

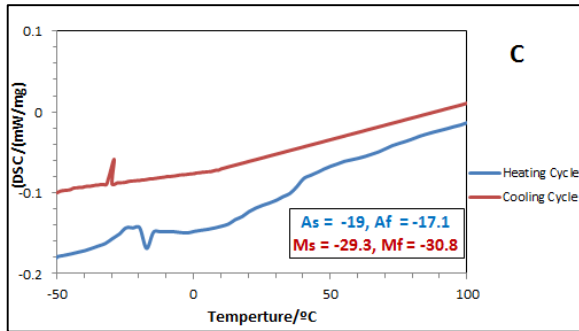


Figure 16. Typical DSC curve for C alloy.

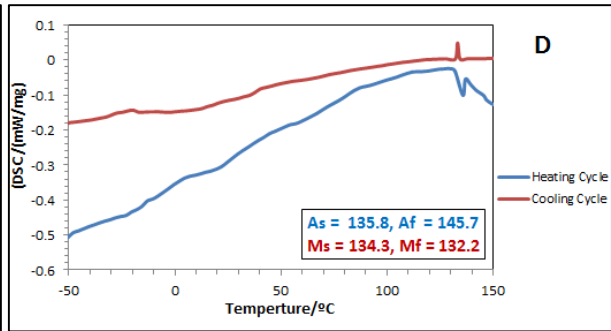


Figure 17. Typical DSC curve for D alloy.

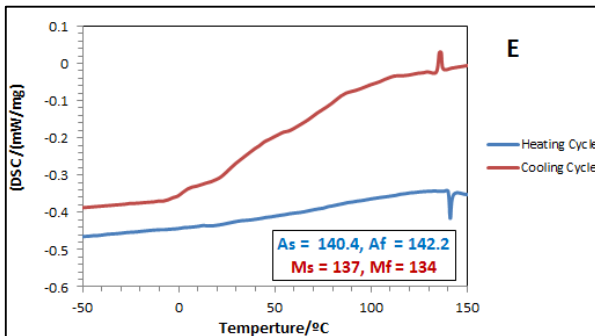


Figure 18. Typical DSC curve for E alloy.

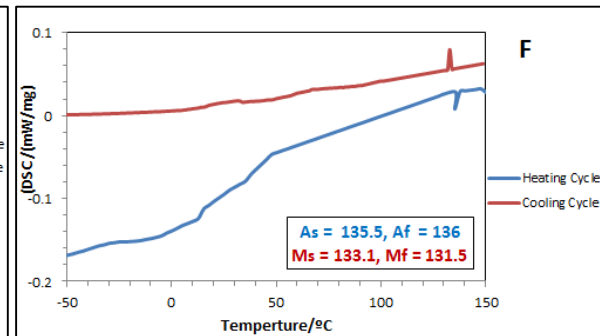


Figure 19. Typical DSC curve for F alloy.

Table 3. show Af, Mf, As and Ms

Alloys	As [°C]	Af [°C]	Ms [°C]	Mf [°C]	Range of M. Trans.(As-Mf) [°C]	Temp.hysteresis (Af -Ms) [°C]
A	14.3	14.6	-4.5	-5.8	20.1	19.1
B	-7	-6.7	-20.5	-21.8	14.8	13.8
C	-19	-17.1	-29.3	-30	11	12.2
D	135.8	145.7	134.3	132.2	3.6	11.4
E	140.4	142.2	137	134	6.4	5.2
F	135.5	136	133.1	131.5	4	2.9

4.3.2. Shape memory Effect

In the shape memory effect (SME%) of A, B, C, D, E and F alloys, the treatment was determined by using microhardness by measuring the diameter of ball indenter after and before the heat treatment by two different temp, which are (50 and 150) °C as shown in table (4) which is far less than 5% [22]. The highest shape memory effect was achieved when the lower nb content shape memory effect was observed in Ti-(13,14,15) at% Nb higher than in Ti-(23, 24, 25) at%Nb and this result conforms with other works, such as Lai et al.'s [21,30,31].

5. Mechanical Test

5.1. micro hardness Test

The hardness values of all alloys studied in this work increase as the niobium content increases, as seen in Figure (20). Whereas, the hardness of (Ti-13Nb) alloy is 336.78 while (Ti-25Nb) alloy is 560.65. This action is connected to strengthening by solid solution, that is significantly impacted by an atom's radius and the number of valence electrons present in the solute atoms [23,24]. This change indicates a strong bonding force between the structure and

the particle which lead to strengthening by preventing lattice movement [25].

5.2. Compression Test

Figure (21) illustrates the results of the compression test, which all specimens passed. Because niobium has a high density (The density of niobium (8.57 g/cm³) slightly differs from Titanium (4.50 g/cm³), the porosity content of the alloy drops while its density rises, thus the compressive strength increases[26, 32,33]. In the Ti-xNb alloys studied, the increasing Nb content resulted in an increase in yield strength [27, 34,35].

Table 4. The Influence of Nb content on SME of Ti-xNb

Synthesized Composition	Code	SME% At 50 °C	SME% At 150 °C
Ti-13Nb	A	4.16	3.73
Ti-14Nb	B	4.11	3.8
Ti-15Nb	C	3.60	4.04
Ti-23Nb	D	2.59	3.2
Ti-24Nb	E	2.6	3
Ti-25Nb	F	3.3	3.5

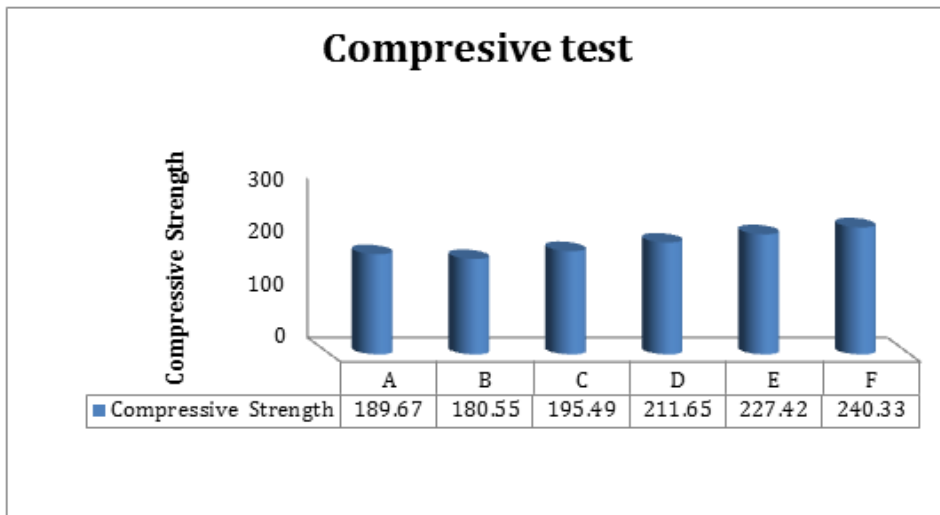


Figure 20. The values of the hardness of alloys A, B, C, D, E and F.

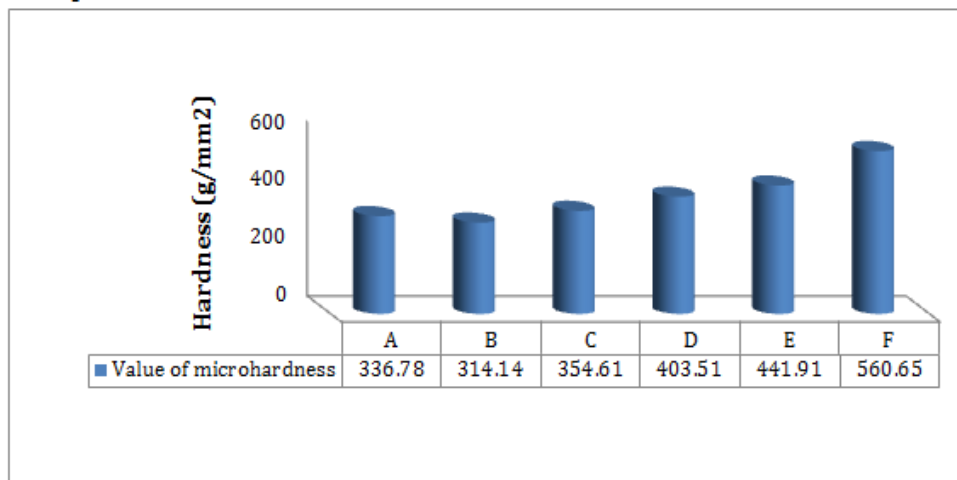


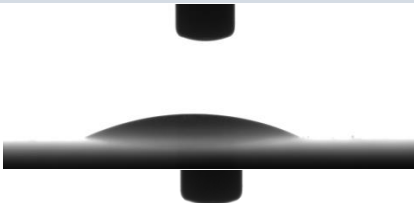





Figure 21. Compression strength for all alloys.

5.3. Contact Angle test

Contact angle is measured to determine the wetting ability of surfaces. It was indicated that the contact angle is greatly affected by the phases and alloying elements [28, 36,37], so the microstructure can be controlled as well as in the contact angle, in this work the microstructure was controlled by change Nb element to the base alloy in different proportions which leads to the spread of the beta phase on the surface of the alloys and thus the contact angle is also controlled. The liquid-solid contact angle (CA) was used to quantify the wetting performance (Table 5). The Ti-25Nb group displayed significantly increased hydrophilicity and lowest CA (33.8 °). remarkably, the

average CA illustrated a decline and the hydrophilicity was improved as the content of niobium (Nb) in Ti-Nb alloys increased. The beta phase creates a thicker oxide layer on the alloy's surface, which decreases the contact angle on the surface. Its biocompatibility increases thus the contact angle decreases and the osseointegration increases. Because the wettability of the oxide layer is influenced by its chemical composition, the thicker oxide layer causes the contact angle values of the samples to decrease as it forms, and the chemical composition of the surface determines the contact angle of the material. The characteristics of the oxide layer on the surface of Ti-Nb alloys are associated to their exceptional biocompatibility [28, 38,39].

Table 5. Value of contact angle for all alloys in the Hank's solution.

Sample	Value of Contact angle	Contact angle Hank's solution
A	56.4	
B	45.65	
C	38.30	
D	36.49	
E	34.8	
F	33.8	

5.4. Electrochemical Tests.

The microstructure of Ti-Nb alloys consist of (β , α'') phases . It is evident that Ti-13Nb produced in this study has a lower corrosion rate than Ti-25Nb alloys. These findings demonstrated the beneficial effects of the Nb content on the corrosion behavior of β -phase titanium alloys. The second generation β -microstructure may play an important role for improving the corrosion resistance.

Figure (22) represents polarization curve for A, B, C, D, E, F alloys in Hanks solution. The figure shows that the alloys which have Nb reduce the current density considerably, leading to an improvement corrosion resistant. In corrosion resistance of the alloy. As indicated in Table (6) the corrosion rate for sample D,E ,F alloy is greater than A, B, C because the corrosion rate affected with

the niobium content and the porosity content decrease also Niobium is a very reactive metal, and its high valence means that it can form more bonds with other atoms, also galvanic corrosion occurs between the two phases. This makes Ti-13Nb alloy a relatively reactive alloy. The equivalent weight of an alloy can be used to predict its corrosion resistance. In general, alloys with higher equivalent weights are more susceptible to corrosion. This is because the higher the reactivity of these alloys, the more likely they react with other substances, such as water and oxygen[23,29].

These results confirmed the effective role of niobium percentage of beta phase in Ti-x% at Nb alloys, also on the resistance to corrosion of the alloy in biological media which mean that the alloys become safer for use inside the human body.

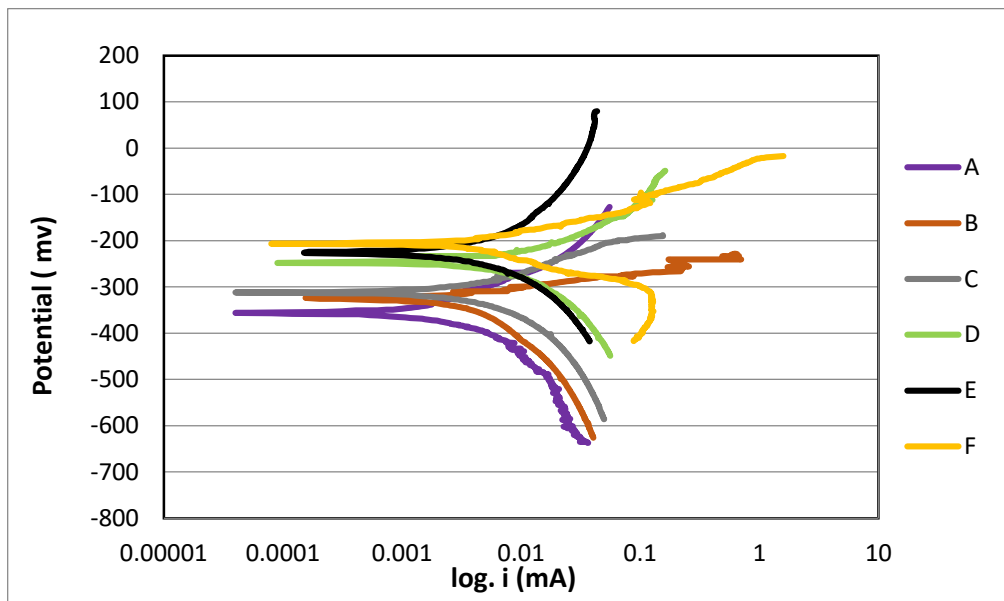


Figure 22. depicts the polarization curve for the alloys in the Hanks solution.

Table 6. Alloys in Hanks Solution at 37°C: Corrosion Current (I_{corr}), Corrosion Potential (E_{corr}), and Corrosion Rate (C.R.)

samples code	Chemical composition (at%)	I_{corr} ($\mu A/ cm^2$)	Potential E_{corr} (mV)	C.R (mpy)
A	87at Ti-13at Nb	1.43	-357	0.274
B	86at Ti-14at Nb	1.01	-327.1	0.267
C	85at Ti-15at Nb	1.28	-313.1	0.334
D	77at Ti-23at Nb	2.46	-247.2	0.62
E	76at Ti-24at Nb	2.86	-224.1	0.716
F	75at Ti-25at Nb	2.96	206.3	0.74

6. Conclusions

In this study, the effects of Nb concentrate on the microstructure and mechanical properties of Ti-xNb alloys were investigated. The results supported the following claims:

- Due to the existence of the β phase, the mechanical characteristics of Ti-xNb ($x=13, 14, 15, 23, 24$ and 25) at% vary on the Nb concentration. owing to their enhanced mechanical characteristics and equivalent biological function.
- It appears that sintering prepared samples for seven hours at 1300°C is a very effective way to ensure that Ti and Nb are entirely sinterable into the resulting structure.
- The hardness of Ti-Nb produced alloys increased proportionately with an increase in niobium percentage.
- The Ti-Nb alloys are a good possibility for implantable medical devices; nevertheless, because of their alloys' greater transformation temperatures than those of humans, shape memory phenomena should be employed with caution.
- The maximum shape effect (4.16 %) are founded in the A (Ti-13Nb) alloy.
- F(Ti-25Nb) alloy have higher values of the corrosion rate compared with the other alloys.

References

- [1] Otsuka K. and Wayman C.M., "Shape Memory Materials", Cambridge University Press, 1998.
- [2] M. Niinomi, Metall. "RECENT METALLIC MATERIALS FOR BIOMEDICAL APPLICATIONS", Mater. Trans. Vol. 33, No. 5, 2002, pp.477-486.
- [3] J.I. Kim, H.Y. Kim, T. Inamura, H. Hosoda, and S. Miyazaki, Shape Memory Characteristics of Ti-22Nb-(2-8)Zr(at.%) Biomedical Alloys, Mater. Sci. Eng. Vol. 403, 2005, pp. 334–339.
- [4] Qu W, Sun X, Yuan B, Xiong C, Zhang F, Li Y, Sun B., "Microstructures and phase transformations of Ti-30Zr-xNb ($x = 5, 7, 9, 13$ at.%) shape memory alloys", Mater. Charact. Vol.122, 2016, pp.1–5.
- [5] X. Tang, T. Ahmed, H.J. Rack, J. "Phase transformations in Ti-Nb-Ta and Ti-Nb-Ta-Zr alloys", Mater. Sci. Vol. 35, 2000, pp. 1805-1811.
- [6] Y.L. Hao, S.J. Li, S.Y. Sun, R. Yang, "Controlling reversible martensitic transformation in titanium alloys with high strength and low elastic modulus", Scripta Materialia. Vol. 67, 2012, pp.487-490.
- [7] Hee Young Kim, Yoshinori Ohmatsu, Jae Il Kim, Hideki Hosoda and Shuichi Miyazaki, "Mechanical Properties and Shape Memory Behavior of Ti-Mo-Ga Alloys", Materials Transactions, Vol. 45, No. 4, 2004, pp. 1090 - 1095.
- [8] Hee Young Kim, Hashimoto Satoru, Jae Il Kim, Hideki Hosoda and Shuichi Miyazaki, "Mechanical Properties and Shape Memory Behavior of Ti-Nb Alloys", Materials Transactions, Vol. 45, No. 7, 2004, pp. 2443 to 2448.
- [9] H.Y. Kim, Y. Ikehara, J.I. Kim, H. Hosoda, and S. Miyazaki, "Martensitic Transformation, Shape Memory Effect and Superelasticity of Ti-Nb Binary Alloys", Acta Mater., Vol. 9, No. 54, 2006, pp. 2419– 2429.
- [10] D. Kuroda, M. Niinomi, M. Morinaga, Y. Kato, and T. Yashiro, "Design and Mechanical Properties of New b Type Titanium Alloys for Implant Materials", Mater. Sci. Eng. A, 243(1-2), 1998, pp 244–249.
- [11] H.Y. Kim, S. Hashimoto, J.I. Kim, H. Hosoda, and S. Miyazaki, "Mechanical Properties and Shape Memory Behavior of Ti-Nb Alloys", Mater. Trans., Vol. 7, No. 45, 2004, pp. 2443–2448.
- [12] Damian Kalita, Łukasz Rogal, Tomasz Czeppe, Anna Wo'jcik, Aleksandra Kolano-Burian, Przemysław Zackiewicz, Bogusz Kania, and Jan Dutkiewicz, "Microstructure and Mechanical Properties of Ti-Nb Alloys Prepared by Mechanical Alloying and Spark Plasma Sintering", Journal of Materials Engineering and Performance, 2019.
- [13] H.Y. Kim and S. Miyazaki, "Several Issues in the Development of TiNb-Based Shape Memory Alloys", Shape Mem. Superelast., Vol. 4, No. 2, 2016, pp. 380–390.
- [14] Mehmet Kaya*, Abdurrahman Yolun, Ömer Çakmak, "Mechanical Properties of Ti-18Nb Alloy Fabricated by Powder Metallurgy", Universal Journal of Materials Science, Vol. 3, No. 6, 2018, pp.85-91.
- [15] Jian Zhang, Yanjie Li, and Wei Li, "Metastable phase diagram on heating in quenched Ti-Nb high-temperature shape memory alloys "J Mater Sci ,No.56, 2021, pp.11456–11468.
- [16] de Oliveira CSS, Griza S, de Oliveira MV, Ribeiro AA, Leite MB, "Study of the porous Ti35Nb alloy processing parameters for implant applications", Powder Technol. No.281, 2015, pp. 91–98.
- [17] Kadhim, Abdul –Raheem, "Investigation Of Certain Shape Memory Alloys In Space Systems", PhD thesis. University of Babylon, College of Engineering, 2007.
- [18] Khilfa, A. H., "Effect of Y and Ge addition on Mechanical properties and Corrosion behavior of Biomedical CoCrMo Alloy (F75) ", MSc thesis, University of Babylon, Iraq, 2015.
- [19] Saud SNet al Corrosion and bioactivity performance of graphene oxide coating on TiNb shape memory alloys in simulated body fluid Mater. Sci. Eng.C68, 2016, pp. 687–94.,
- [20] H.Y. Kim, Y. Ikehara, J.I. Kim, H. Hosoda, and S. Miyazaki, "Martensitic Transformation, Shape Memory Effect and Superelasticity of Ti-Nb Binary Alloys", Acta Mater., V. 9, No.54, 2006, PP 2419– 2429.
- [21] M. Lai, Y. Gao, B. Yuan, and M. Zhu, Remarkable , "Superelasticity of Sintered Ti-Nb Alloys by Ms Adjustment Via Oxygen Regulation", Mater. Des., 87, 2015 pp 466–472.
- [22] B. L. Wang, Y. F. Zheng and L. C., " Electrochemical corrosion behavior of biomedical Ti–22Nb and Ti–22Nb–6Zr alloys in saline medium", No. 10,2009, pp.60.
- [23] R.Prakash kolli and Arun Devarai "A Review of Metastable Beta Titanium Alloys", *Metals Vol.7*, No.8, 2018, pp.506.
- [24] M.S. Kaiser, M.K. Banerjee, "Effect of Ternary Scandium and Quaternary Zirconium and Titanium Additions on the Tensile and Precipitation Properties of Binary Cast Al-6Mg Alloys", Jordan Journal of Mechanical and Industrial Engineering, Vol. 2, No. 2, 2008, pp. 93 – 99.
- [25] Ramadan J. Mustafa, "Temperature Dependence of Dynamic Modulus and Damping in Continuous Fiber- Reinforced Al-(alloy) Matrix Composites at Elevated Temperatures", Jordan Journal of Mechanical and Industrial Engineering, Vol. 2, No. 1, 2008, pp. 15 – 21.
- [26] Moh'd Sami" S. Ashhab , "Application of Neural Net Modeling and Inverse Control to the Desulphurization of Hot Metal Process", Jordan Journal of Mechanical and Industrial Engineering, Vol. 1, No. 2, 2007, pp. 79 – 84.
- [27] H.Y. Kim, J.I. Kim, T. Inamura, H. Hosoda, and S. Miyazaki, "Effect of Thermo-mechanical Treatment on Mechanical Properties and Shape Memory Behavior of Ti-(26-28) at.% Nb Alloys", Mater. Sci. Eng. A, 438, 2006, pp 839–843.
- [28] Yuqing Zhang, Danni Sun, Jun Cheng, James Kit Hon Tsoi, Jiang Chen, "Mechanical and biological properties of Ti–(0–25 wt%)Nb alloys for biomedical implants application" *Regenerative Biomaterials*, Vol. 7, No. 1, 2020, pp 119–127,

- [29] Sura Ali Shahee, Ekbal mohammed Saeed, Nabaa Sattar Radhi "Ni-Free Ti- Based Shape Memory Alloys: Review", AIP Conf. Proc. NO. 3009, 2024, pp. 030041-1–030041-7.
- [30] Jeyanthi, S. "A Comparative Analysis of Flexible Polymer-Based Poly (vinylidene) Fluoride (PVDF) Films for Pressure Sensing Applications." *JJMIE* 17.3 (2023).
- [31] Zhang, Qian, Huang Tang, and Shihui Guo. "Calculation Method of Stiffness and Deflection of Corroded RC Beam Strengthened by Steel Plate." *Jordan Journal of Mechanical and Industrial Engineering* 15.1 (2021)
- [32] [Azad, Abdul Kalam, "Fabrication of Al-6061/SiC Nano Composite Material Through Ultrasonic Cavitation Technique and Its Analysis." *JJMIE* 17.3 (2023).
- [33] Asmael, Mohammed, OtonyeTekena Fubara, and Tauqir Nasir. "Prediction of Springback Behavior of Vee Bending Process of AA5052 Aluminum Alloy Sheets Using Machine Learning." *Jordan Journal of Mechanical and Industrial Engineering* 17.1 (2023).
- [34] Damseh, Rebhi A. "Chemically Reactive Nanofluid Flowing across Horizontal Cylinder." *Jordan Journal of Mechanical and Industrial Engineering* 17.1 (2023).
- [35] Ekpruke, E. O., C. V. Ossia, and A. Big-Alabo. "On the Morphological and Tribological Characterization of Green Automotive Brake Pads Developed from Waste Thais Coronata Seashells." *Jordan Journal of Mechanical and Industrial Engineering* 17.2 (2023).
- [36] Ali, Raad Mohammed Kadhim, and Sajida Lafta Ghashim. "Thermal performance analysis of heat transfer in pipe by using metal foam." *Jordan Journal of Mechanical and Industrial Engineering* 17.2 (2023).
- [37] Nafteh, MassoumehAzizi, and Mahmoud Shahrokhi. "Improving the COPRAS Multicriteria Group Decision-Making Method for Selecting a Sustainable Supplier Using Intuitionistic and Fuzzy Type 2 Sets." *Jordan Journal of Mechanical and Industrial Engineering* 17.2 (2023).
- [38] Sadashiva, K., and K. M. Purushothama. "Investigation on Mechanical and Morphological Characteristics of Ramie/Silk with Epoxy Hybrid Composite of Filler OMMT Nanoclay." *Jordan Journal of Mechanical & Industrial Engineering* 17.2 (2023).
- [39] Balcha, Robson, Perumalla Janaki Ramulu, and Belay Brehane Tesfamariam. "Mechanical Behaviour Assessment of Banana Fibres Reinforced Polymeric Composite with Aluminium-Powder Filler." *Jordan Journal of Mechanical and Industrial Engineering* 17.2 (2023).